

# Earth and Space Science



## RESEARCH ARTICLE

10.1029/2021EA001670

## Characterization of the Candidate Landing Region for Tianwen-1—China's First Mission to Mars

### Key Points:

- Topographic, geomorphological, and geologic characterization of the candidate landing region of Tianwen-1
- A hazard map of the region combining engineering constraints on slopes, crater density, cone density, and rock abundance
- Two local areas in the region are highlighted as potential landing sites for their low hazard and scientific significance

### Supporting Information:

Supporting Information may be found in the online version of this article.

### Correspondence to:

B. Wu and J. Dong,  
[bo.wu@polyu.edu.hk](mailto:bo.wu@polyu.edu.hk);  
[donghn13@163.com](mailto:donghn13@163.com)

### Citation:

Wu, B., Dong, J., Wang, Y., Li, Z., Chen, Z., Liu, W. C., et al. (2021). Characterization of the candidate landing region for Tianwen-1—China's first mission to Mars. *Earth and Space Science*, 8, e2021EA001670. <https://doi.org/10.1029/2021EA001670>

Received 20 JAN 2021

Accepted 9 MAY 2021

Bo Wu<sup>1</sup> , Jie Dong<sup>2</sup>, Yiran Wang<sup>1</sup>, Zhaojin Li<sup>1</sup> , Zeyu Chen<sup>1</sup>, Wai Chung Liu<sup>1</sup> , Jiaming Zhu<sup>1</sup>, Long Chen<sup>1</sup> , Yuan Li<sup>1</sup>, and Wei Rao<sup>2</sup>

<sup>1</sup>Planetary Remote Sensing Laboratory, Department of Land Surveying and Geo-Informatics, The Hong Kong Polytechnic University, Hong Kong, P.R. China, <sup>2</sup>China Academy of Space Technology, Beijing, P.R. China

**Abstract** This paper presents our efforts to characterize the candidate landing region (109°–133°E, 23°–30°N) for Tianwen-1, China's first mission to Mars, in terms of engineering safety and scientific significance. Topographic analysis reveals that the region has a low elevation around  $-4,230$  m, and 98% of the region have slopes smaller than 8°. The geomorphological mapping and analysis show that the region has an average crater density of about 28 craters ( $\geq 200$  m in diameter) per 100 square kilometers, with several clusters of high crater densities distributed around the center of the region. There are also pitted cones distributed mainly in the southern part of the region, with a density of approximately 6.6 cones per 100 square kilometers in specific local areas. The region has rock abundances ranging from 1% to 23%, with local clusters of low and high rock abundances. The region comprises four main geological units, including a lowland unit formed in the Late Hesperian and a volcanic unit formed in the Amazonian and Hesperian period. Their specific surface ages are estimated through the analysis of crater size-frequency distribution. Combining the engineering constraints on surface slopes, crater density, cone density, and rock abundance, a hazard map of the candidate landing region is generated for landing site evaluation and safety assessment. Based on the results, we further discuss the potential scientific outcomes from the exploration in this region. The findings will be helpful for the mission planning and maximization of the scientific return from Tianwen-1, and complement existing Martian scientific research.

## 1. Introduction

China's first Mars probe, named Tianwen-1, which means “heavenly questions” in Chinese, was successfully launched on July 23, 2020, from the Hainan Island in Southern China. The Tianwen-1 probe comprises an orbiter and a lander/rover composite, and aims to complete orbiting, landing, and roving in one mission (Ye et al., 2017). The probe successfully entered orbit on February 10, 2021. The lander/rover will perform a soft landing on the Martian surface 2–3 months after the arrival of the probe, and the orbiter will remain in orbit to provide a relay communication link to the rover while performing its own scientific observations (Wan et al., 2020). With the scientific payloads onboard both the orbiter and rover, Tianwen-1 will investigate the Martian surface and sub-surface for its scientific objectives including: (1) the mapping of the morphology and geological structure, (2) the investigation of the surface soil characteristics and water-ice distribution, (3) the analysis of the surface material composition, (4) the measurement of the ionosphere and the characteristics of the Martian climate and environment, and (5) the analysis of the physical fields and internal structure of Mars (Wan et al., 2020; Zou et al., 2021).

As indicated in Grant et al. (2018) and Pajola et al. (2019), the identification of a Mars landing site is a complex process that involves both engineering safety and scientific importance. This is also true for the selection of a candidate landing region for Tianwen-1's lander/rover. The Tianwen-1 rover (Jia et al., 2020) is about 1.85 m high, 2 m long, and weighs about 240 kg. The rover has six wheels, each has a diameter of 30 cm and is 20 cm wide. The height of its carriage bottom from the ground (i.e., rover ground clearance) is 30 cm (Pan et al., 2020). It has four solar panels and mainly relies on solar energy to charge the batteries of the onboard instruments. The rover is designed with an expected 90 sols (Martian days) lifetime, and can travel on the Martian surface at a speed of about 200 m per hour. The scientific objectives of the rover include: (1) investigation of topography and geological structure of the roving area, (2) surveying of the soil structure of the roving area and searching for water ice, (3) analysis of elements, minerals and rock

© 2021. The Authors. Earth and Space Science published by Wiley Periodicals LLC on behalf of American Geophysical Union.

This is an open access article under the terms of the [Creative Commons Attribution-NonCommercial-NoDerivs License](https://creativecommons.org/licenses/by-nc-nd/4.0/), which permits use and distribution in any medium, provided the original work is properly cited, the use is non-commercial and no modifications or adaptations are made.

**Table 1**  
*General Engineering Requirements for Landing Region Evaluation*

Parameter	Requirement
Latitude	5°–30°N
Elevation	≤−3 km with respect to MOLA geoid
Slopes	≤8°
Rock abundance	≤7%
Crater/cone distribution	A low density
Thermal inertial	≥150 Jm <sup>−2</sup> s <sup>−0.5</sup> K <sup>−1</sup>
Albedo	0.1 ≤ Albedo ≤ 0.26

Abbreviation: MOLA, Mars Orbiter Laser Altimeter.

types of the roving area, and (4) investigation of physical characteristics of the atmosphere and the surface environment of the roving area (Zou et al., 2021). Table 1 lists the general engineering requirements for considering possible landing regions.

The selection of a candidate landing region for Tianwen-1's lander/rover consisted of multiple steps. In the first step, three candidate regions located within the latitude ranges of 5°–30°N were selected, based on engineering constraints such as adequate solar illumination for optimized power generation and moderate temperature, lower elevation for longer deceleration time, and a flat terrain surface for safer landing (Dong et al., 2019). These three candidate regions are located on the large *planitiae* (plains) on Mars, namely Amazonis Planitia, Chryse Planitia, and Utopia/Isidis Planitia, as shown by the red dashed polygons on the color shaded relief of the Mars Orbiter Laser Altimeter (MOLA, Smith et al., 2001) data in Figure 1a.

In the second step, the region on Amazonis Planitia was excluded due to its small thermal inertias (55.5 Jm<sup>−2</sup>s<sup>−0.5</sup> K<sup>−1</sup> in average) and heavier dust cover (Putzig et al., 2005). In the third step, the remaining two regions were analyzed in detail in terms of elevations, slopes, rock abundances, crater densities, and geological context. The region in Chryse Planitia was ruled out due to its rougher terrain surface and interesting (Pajola, Rossato, Baratti, et al., 2016; Sefton-Nash et al., 2015), but complicated geomorphological features. In the Utopia/Isidis Planitia, a region in the southern Utopia Planitia (delineated by the red solid-lined rectangle in Figure 1a) was further selected as the candidate landing region, for its optimal combination of the engineering constraints and scientific importance.

Figure 1b shows an overview of the candidate landing region (109°–133°E, 23°–30°N), which is an image mosaic (6 m/pixel) generated from 260 Mars Reconnaissance Orbiter (MRO) Context Camera (CTX) images using an image ortho-rectification and co-registration method (Hu et al., 2019). Figure 1c shows a geological map (Tanaka et al., 2014) of the candidate landing region and its surrounding area. It is located in the southern part of Utopia Planitia, the largest recognizable plain in the northern lowlands on Mars (McGill, 1989). The third tallest volcano mountain on Mars, Elysium Mons, is approximately 250 km to the east. Nepenthes Planum (a high plain/plateau), which defines the boundary between the sedimentary plains in the north and the cratered highlands in the southern hemisphere, is approximately 500 km to the south.

As shown in Figure 1c, the west part of the candidate landing region represents a lowland unit on Utopia Planitia, formed during the Late Hesperian period. Researchers suggested that Utopia Planitia possibly contained ponded water/ice in Late Hesperian (Chapman, 1994; Ivanov et al., 2014; Scott et al., 1992). Some lowland areas on Utopia Planitia might be formed by the degradation of ice-rich permafrost (Sejourne et al., 2012). The east part of the candidate landing region sits on volcanic units that resulted from the Elysium Mons in the east formed during the Late Amazonian period (Vaucher et al., 2009). The lava fields of Elysium Mons have distinct geochemical and temporal differences between its southeastern and northwestern fields (Susko et al., 2017). The remote sensing and in situ investigations in the candidate landing region by the instruments onboard the Tianwen-1 orbiter and lander/rover may bring new insights on the existence and history of water/ice in this region as well as the magmatism characteristics on Mars.

## 2. Topographic Characteristics of the Candidate Landing Region

Figure 2a shows a digital elevation model (DEM) of the candidate landing region generated from the MOLA data with a spatial resolution of 463 m/pixel. The region features a low elevation ranging from −6,038 to −3,275 m, with an average elevation of −4,230 m and a standard deviation of 189.5 m. It can be seen from Figure 2a that the region is mainly flat, when considering a baseline of 463 m, except for some craters, channels, and ridges distributed in the region.

Based on the MOLA DEM, surface slopes within the candidate landing region were calculated and analyzed. Surface slopes are the gradients of the elevations calculated at a specific baseline. For any point in the

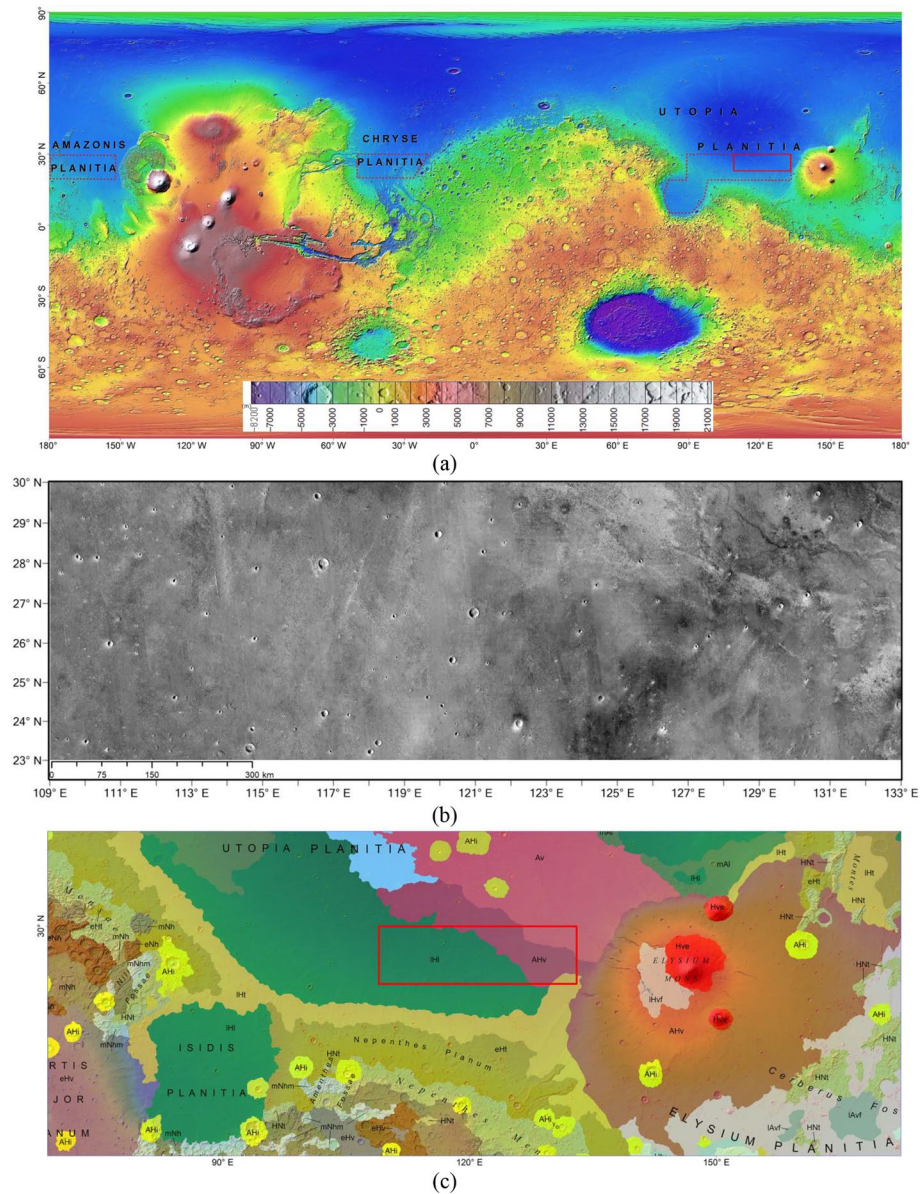


**Figure 1.** The candidate landing region of Tianwen-1. (a) Three candidate regions (red dashed lines) and the selected candidate landing region (red solid lines) shown on a global color-shaded relief of MOLA data; (b) A CTX image mosaic (6 m/pixel) of the candidate landing region (109°–133°E, 23°–30°N); (c) A geological map (Tanaka et al., 2014) showing the selected candidate landing region and its surrounding area overlaid on the MOLA shaded relief.

gridded DEM, slopes along the horizontal and vertical directions are calculated, based on the distance and elevation difference of at least two neighboring grid cells; and the square root of the sum of their squares is determined as the maximum slope at that point. Figure 2b shows the slope map of the region derived from the MOLA DEM with a baseline of 926 m (two pixels in the DEM). It reveals an average slope of 0.5°, with the maximum slope of 37.9° and a standard deviation of 1.4°. The majority of the region has surface slopes less than 2°. Large slopes are mainly distributed around craters, channels, and ridges.

Slopes will also need to be analyzed at a baseline similar to the lander footprint size for surface hazard evaluation, which is 4 m in this research. However, slope analysis at the 4-m baseline requires DEMs of higher resolution in meters. There are several DEMs (about 100 m/pixel resolution) generated from Mars Express's High Resolution Stereo Camera (HRSC) images within the candidate landing region. However, they only cover small segmented areas in the region. There is no higher resolution DEMs from CTX images

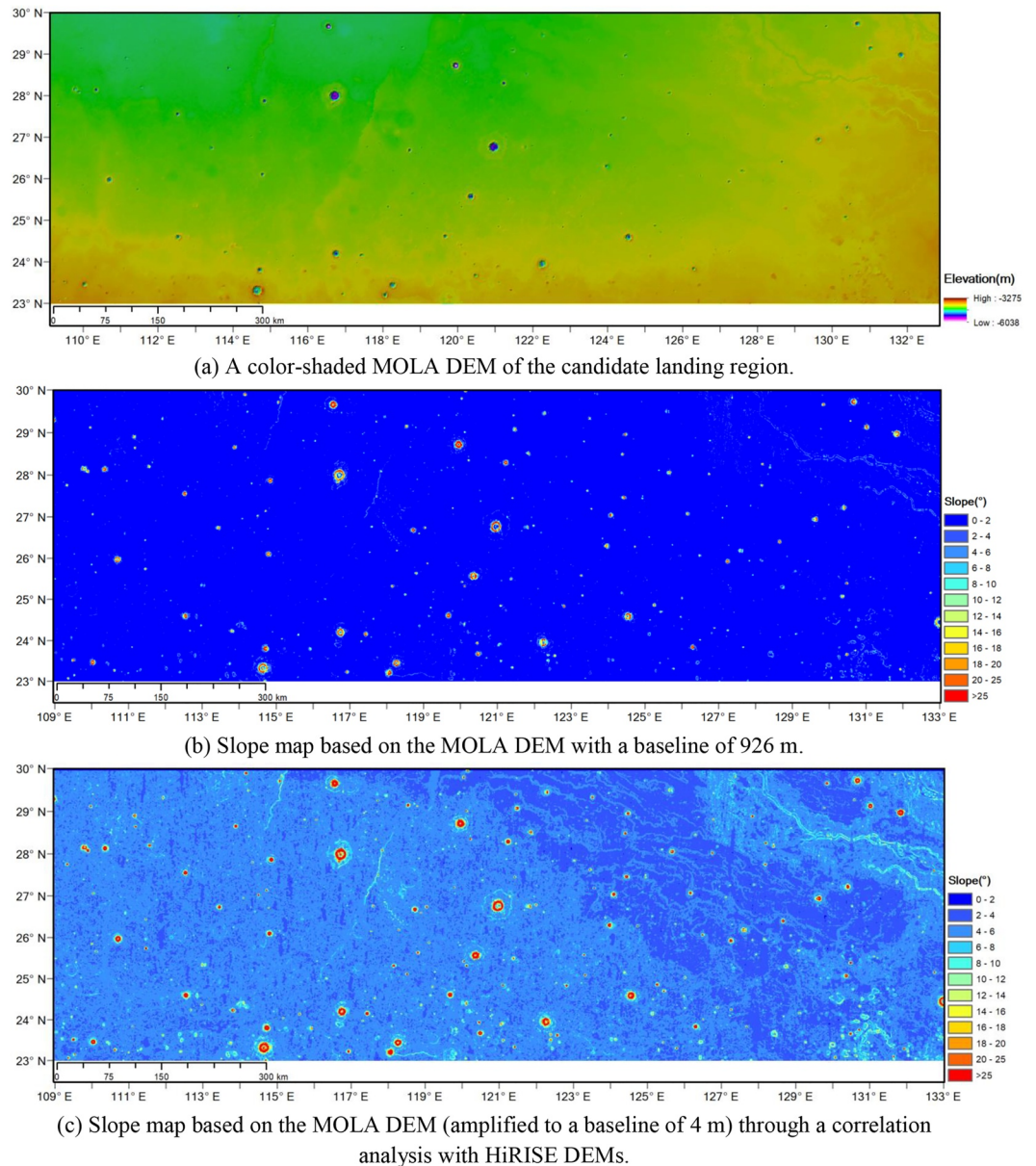


**Figure 2.** The digital elevation model (DEM) and slope maps of the candidate landing region. (a) A color-shaded Mars Orbiter Laser Altimeter (MOLA) DEM of the candidate landing region. (b) Slope map based on the MOLA DEM with a baseline of 926 m. (c) Slope map based on the MOLA DEM (amplified to a baseline of 4 m) through a correlation analysis with High Resolution Imaging Science Experiment DEMs.

available in this region. The images collected by the High Resolution Imaging Science Experiment (HiRISE) onboard MRO offer a spatial resolution of 0.3 m/pixel, which can be used to generate meter-resolution DEMs. However, there are only few stereo pairs of HiRISE images in the candidate landing region. In our previous research (Wang & Wu, 2017), we presented a correlation analysis of slopes derived from DEMs with different resolutions of the same terrain surface on Mars. First, slope maps were derived from HiRISE DEMs (meter-level resolution) and a series of down-sampled HiRISE DEMs. The latter was used to simulate low-resolution DEMs. Then the high-resolution slope map was down-sampled to the same resolution as the slope map from the lower resolution DEMs. Thus, a comparison could be conducted between them pixel by pixel. For each pixel on the slope map from the lower resolution DEM, it could reach a similar slope with the down-sampled HiRISE slope by multiplying an amplifying factor. Seven sets of HiRISE images with representative terrain types were used for correlation analysis, which revealed that the relationship between

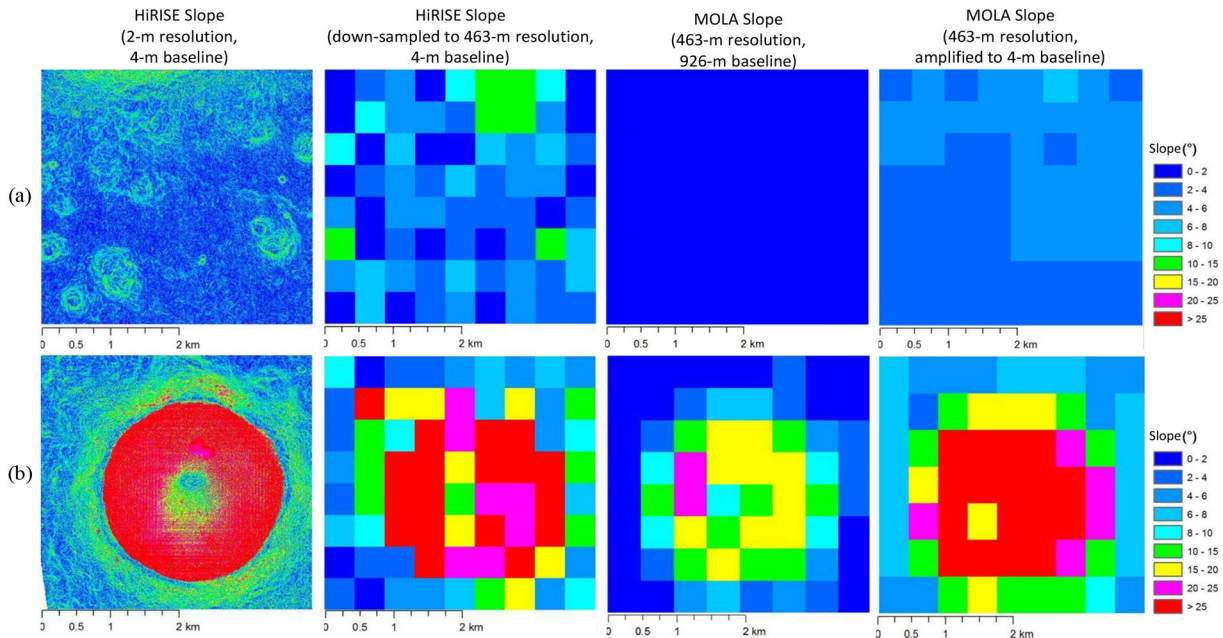


**Figure 3.** Analysis of slopes at different baselines based on High Resolution Imaging Science Experiment (HiRISE) and Mars Orbiter Laser Altimeter (MOLA) digital elevation models (DEMs) covering the same local areas in the candidate landing region. (a) A relatively flat area; (b) A crater area.

the amplifying factors and the original MOLA slopes could be described by an exponential function. Verifications using DEMs from HiRISE and CTX images and MOLA datasets showed that after applying the amplifying function, the updated MOLA slope maps better represented slopes in short baselines (e.g., 4 m for HiRISE DEMs and 40 m for CTX DEMs) compared with the original slopes (926 m baseline for MOLA DEMs). The same method was used here for the estimation of slopes at different baselines. DEMs with a resolution of 2 m/pixel were generated from the stereo pairs of HiRISE images available in the region. MOLA DEMs were clipped to cover the same area as the HiRISE DEMs. They were then used for correlation analysis of slopes at baselines of 4 and 926 m, respectively. A slope amplification function was obtained from the correlation analysis, which provides different multipliers for different slopes at the longer baseline so that to reduce their differences with those calculated at the shorter baseline. Figure 3 shows examples of the correlation analysis of slopes at two representative terrain types (a crater area and a relatively flat area) in the candidate landing region. The average difference of slopes between the one calculated using the HiRISE DEM at the 4-m baseline and the one from MOLA DEM at the 926-m baseline is  $3.8^\circ$  for the relatively flat area. For the crater area, however, the average difference of slopes reaches  $9.5^\circ$ , indicating slopes are influenced more by baselines on more fluctuant terrain surfaces. After applying the slope amplification function, the average differences of slopes are reduced to  $1.3^\circ$  and  $2.2^\circ$  for the relatively flat area and the crater area, respectively, indicating the mean errors for slopes on different terrain types estimated by this method.

It should be noted that, there are some limitations in the above estimation of slopes at a short baseline by applying an amplification function to the slopes at a longer baseline. For example, the performance of the approach is dependent on the resolution and precision of the slope map of the long baseline. Local deviations from the amplification function may lead to imperfect slope amplification in local areas. Nevertheless, it provides a way for evaluating the surface slopes at a short baseline in a large region, where the coverage of high-resolution DEMs is limited and slopes can only be calculated at a long baseline. It is also meaningful for slope analysis over a large region, as in this case the statistics of slopes on a macro scale for landing site evaluation is emphasized rather than the detailed slopes in local scales.

Figure 2c shows the slope map with a baseline amplified to 4 m, generated by using the slope amplification function based on the MOLA DEM. It shows more topographic details compared with the one shown in Figure 2b, even though both have the same color legend for slopes. Figure 2c reveals an average slope of

4.6°, with the maximum slope of 65° and a standard deviation of 2.3°. The majority of the region has slopes less than 8°. Similarly, large slopes are mainly distributed around craters, channels, and ridges.

### 3. Geomorphological Characteristics of the Candidate Landing Region

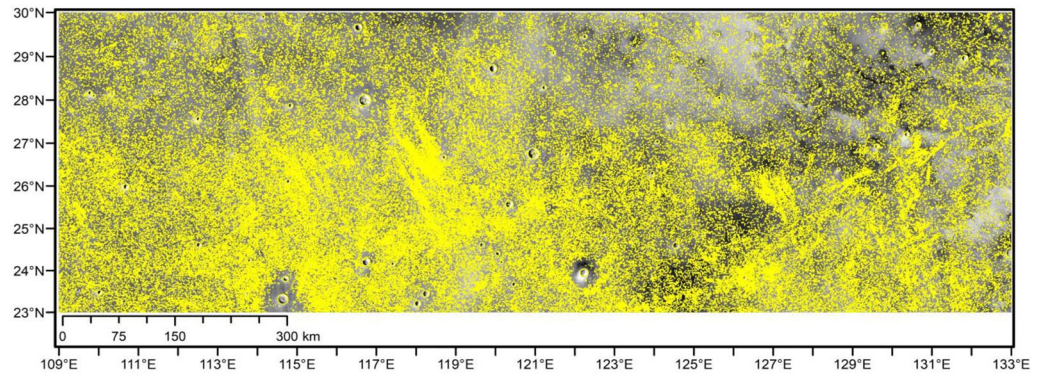
#### 3.1. Crater Distribution

Craters are considered as possible hazards in the landing-site evaluation due to their internal slopes and protuberant rims (Brady et al., 2009), especially for relatively young craters (Erkeling et al., 2012; Ivanov et al., 2020; Pajola, Rossato, Carter, et al., 2016). The more the craters are distributed in a region, the more dangerous is the terrain surface, which will reduce the flexibility in hazard avoidance during the descent phase of the lander. The crater size-frequency distribution (CSFD) also provides useful information for inferring the age of the Martian surface (Ivanov, 2001; Werner, 2014).

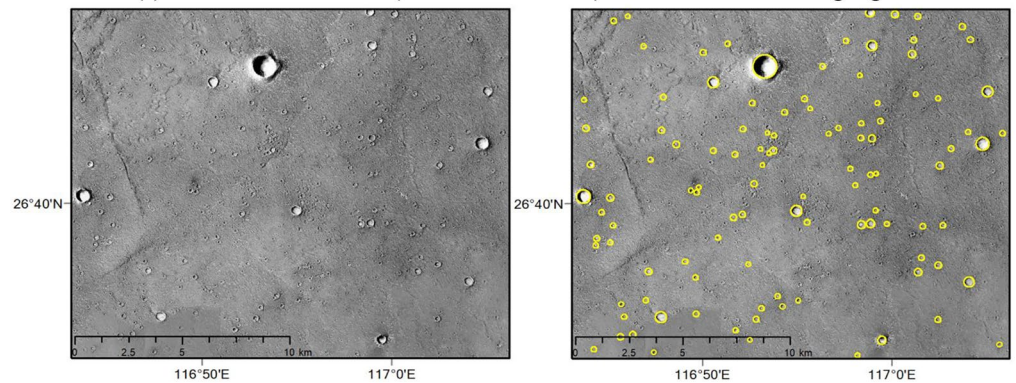
An active machine-learning approach (Wang & Wu, 2019) was developed and used for automatic crater detection on the CTX image mosaic in this research. This approach involved two processes: training and detection. The training process began with a classifier trained using dozens of manually identified positive samples (craters) and negative samples (non-craters). This classifier was then applied to the image to generate an initial set of crater-detection results. Next, annotations for the detection results were requested, with extra 3D information derived from the corresponding MOLA DEM and DEMs (with a spatial resolution ranging from 75 to 100 m per pixel) generated from Mars Express's High Resolution Stereo Camera (HRSC) data in local areas. For each detection result, four profiles (one in vertical, one in horizontal, and two in diagonal directions) were derived from the corresponding DEMs. If all the extracted profiles were in concave shapes (see Figure S1), it was classified as a positive result; otherwise, it was classified as a negative result. Based on the feedback, the annotated results were then added to the positive and negative training samples, respectively. Thus, the training pool was updated and enriched. After several iterations, thousands of positive and negative samples can be automatically generated, allowing the classifier to be retrained to achieve better performance. The final trained classifier was used for automatic crater detection on the images in the region. The active machine-learning approach has a detection rate of about 90% on surface images of Mars for craters with diameters of  $\geq 20$  pixels on the image (Wang & Wu, 2019); however, the detection rate will be decreased for smaller craters. Therefore, in this research, we aimed to use the active machine-learning approach to detect craters with diameters of  $\geq 200$  m based on the CTX image mosaic to ensure the best detection performances. To guarantee the correctness and completeness of the final detected craters, a manual checking process was further performed by several independent operators, using a grid with a cell size of  $200 \times 200$  m overlaid on the CTX image mosaic, to remove artifacts and digitize missing craters. This manual checking process accounted for about 10% of the total number of detected craters.

Finally, a total of 153,183 craters with diameters ranging from 200 m to 15 km were detected in the region, as shown by the yellow circles in Figure 4a. Figure 4b shows examples of the detected craters ( $\geq 200$  m in diameter) in a local area in enlarged views. Among all the detected craters, 68% have diameters of 200–300 m; 20% have diameters of 300–400 m; 6% have diameters of 400–500 m, and the rest 6% have diameters of  $> 500$  m. It indicates an exponential growth of crater numbers along with the decrease of the crater size. A crater density map was generated by counting the number of craters in a moving circular window of  $100 \text{ km}^2$ , as shown in Figure 4c. It should be noted that, a larger circular window will generate a more generalized crater density map; while smaller circular windows will generate sharper density maps. Crater density maps using moving circular windows of 50 and  $25 \text{ km}^2$  are provided in Figure S2 for reference. As we are evaluating the crater densities in one local area relative to other areas within the candidate landing region, the influences of different circular windows on the evaluation results can be neglected, as long as the same circular window size is used for the entire region.

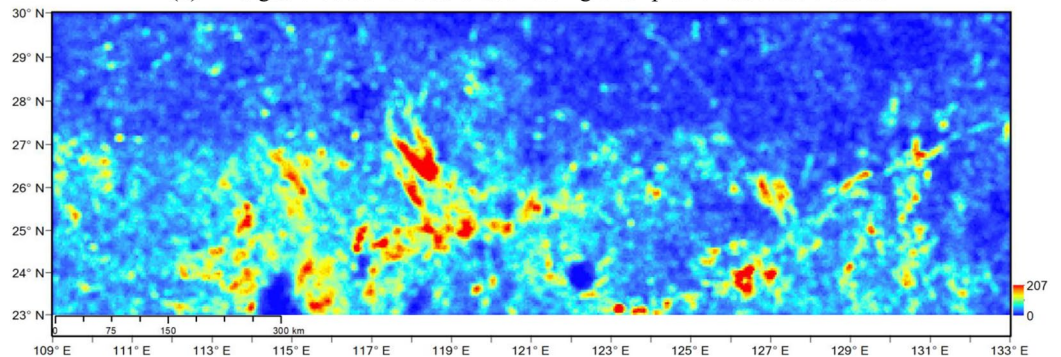
The crater distribution and density maps reveal that craters are concentrated in local regions such as in the central-southern and the southeastern areas of the candidate landing region. The northern area has relatively small crater densities compared with the southern area. The average crater density is approximately 28 craters ( $\geq 200$  m in diameter) per  $100\text{-km}^2$ , and the maximum is 207, which is attributable to a cluster of secondary craters located around the center of the region ( $26.5^\circ\text{N}$ ,  $118.5^\circ\text{E}$ ).



(a) Distribution of craters ( $\geq 200$  m in diameter) in the candidate landing region.



(b) Enlarged views of a local area showing examples of detected craters.



(c) Crater density map (number of craters in a moving circular window of  $100 \text{ km}^2$ ).

**Figure 4.** Crater distribution and density maps in the candidate landing region. (a) Distribution of craters ( $\geq 200$  m in diameter) in the candidate landing region. (b) Enlarged views of a local area showing examples of detected craters. (c) Crater density map (number of craters in a moving circular window of  $100 \text{ km}^2$ ).

### 3.2. Cone Distribution

The presence of small pitted cones on the northern plains of Mars has been widely recognized (Farrand et al., 2005; Frey & Jarosewich, 1982; McGowan & McGill, 2007). Frey and Jarosewich (1982) presented that most of the kilometer to sub-kilometer cones were located in parts of Eastern Acidalia and Utopia-Isidis-Elysium Planitia, based on the investigation using Viking orbiter images. Farrand et al. (2005) investigated the pitted cones in Acidalia Planitia and Cydonia Mensae and found morphological differences associated with latitudes. The pitted cones located in the north of  $40.5^\circ\text{N}$  in Acidalia Planitia were larger and dome-shaped. The southern cones located in Cydonia Mensae ( $30^\circ\text{N}$ – $40^\circ\text{N}$ ) were smaller and cone-shaped. Various origins of these pitted cones have been suggested, such as rootless cones (Bruno et al., 2006), mud volcanoes (Oehler & Allen, 2010), terrestrial Maars (White & Ross, 2011), and pingos (MacKay, 1998). Most of them are related to water or ice (McGowan & McGill, 2007). We also noticed many pitted cones distributed over

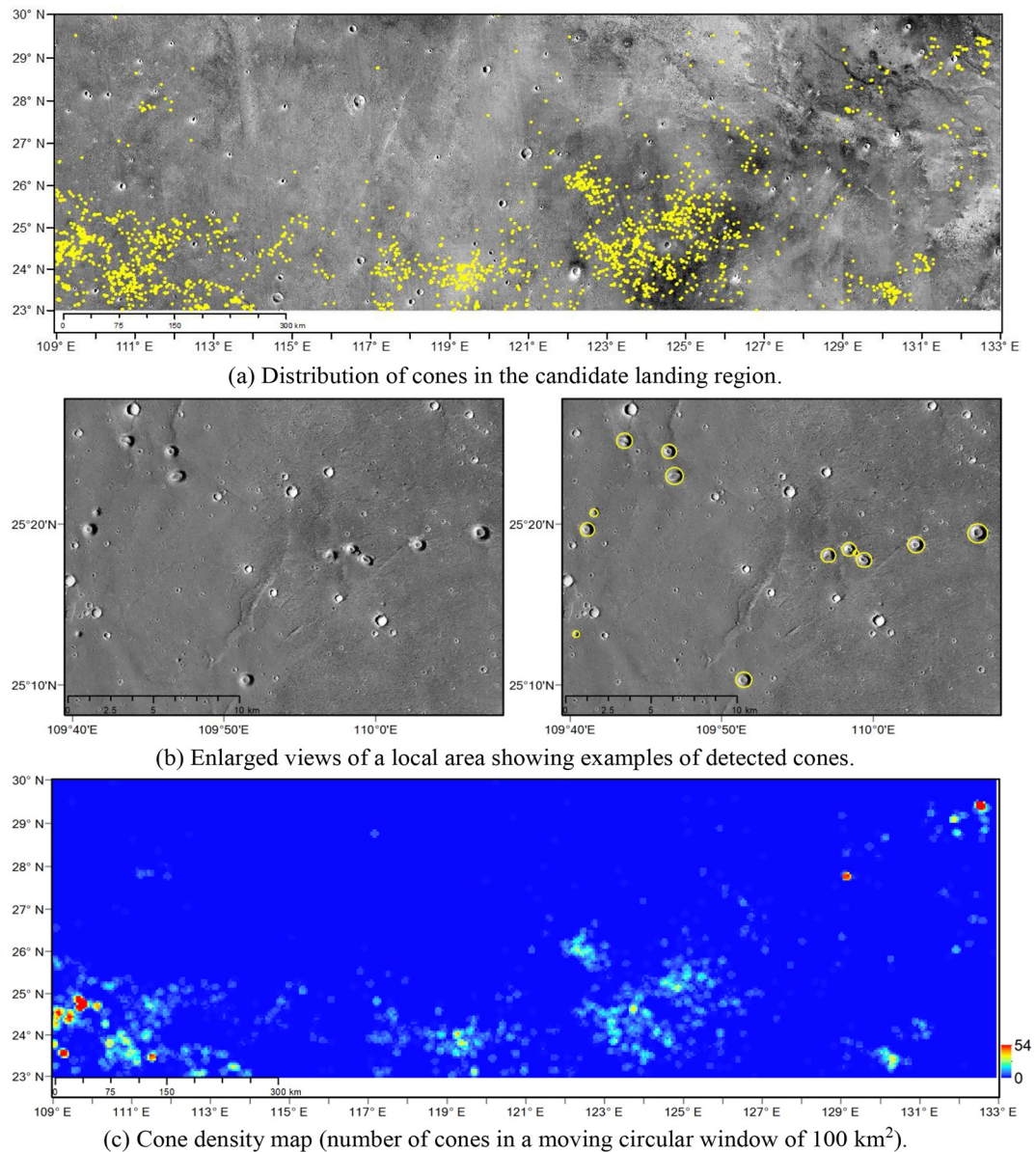
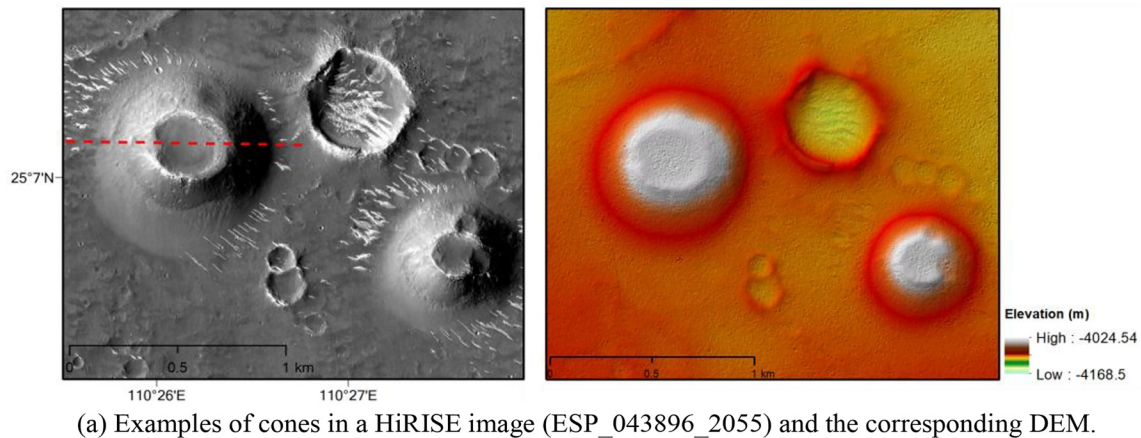


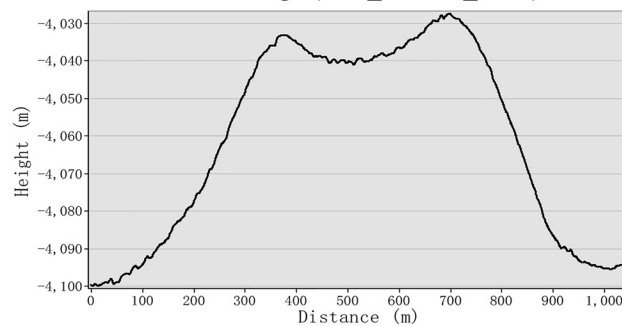
**Figure 5.** Cone distribution and density maps in the candidate landing region. (a) Distribution of cones in the candidate landing region. (b) Enlarged views of a local area showing examples of detected cones. (c) Cone density map (number of cones in a moving circular window of 100 km<sup>2</sup>).

the candidate landing region in the southern part of Utopia Planitia. They are considered as possible hazards in the landing-site evaluation due to their sudden protruding from the terrain surface and steep slopes. Meanwhile, they are also of particular scientific interest as they may indicate the presence of water or ice near the surface (Bruno et al., 2006; McGowan & McGill, 2007).

We manually digitized 2,503 pitted cones visible on the CTX image mosaic, as shown in Figure 5a. Figure 5b shows examples of the detected cones in a local area in enlarged views. Their diameters range from 40 m to 1.7 km, with an average diameter of 550 m. The majority of them have diameters of 400–600 m. The sizes of the cones distributed in this region are similar to those identified in Cydonia Mensae (with a mean diameter of ~542 m) by Farrand et al. (2005). A cone density map was generated by counting the number of cones in a moving circular window of 100 km<sup>2</sup>, as shown in Figure 5c. Similarly, the cone density maps using moving circular windows of 50 and 25 km<sup>2</sup> are provided in Figure S3 for reference. The cone distribution



(a) Examples of cones in a HiRISE image (ESP\_043896\_2055) and the corresponding DEM.



(b) A cone profile along the red dashed line.

**Figure 6.** Examples of cones and cone profile. (a) Examples of cones in a High Resolution Imaging Science Experiment image (ESP\_043896\_2055) and the corresponding digital elevation model. (b) A cone profile along the red dashed line.

and density maps show distinct clusters, mainly distributed in the southwestern and central-southern areas of the region. The northern areas are almost cone free. The representative local areas with moderate cone densities (e.g., the cyan and yellow pixels in Figure 5c) have an average cone density of approximately 6.6 cones per 100-km<sup>2</sup>, and the maximum is 54.

Figure 6a shows examples of these cones in a HiRISE image (ESP\_043896\_2055) with a resolution of 0.3 m/pixel, on which the asymmetric aprons of the cones and their summit pits are clearly visible. The right panel in Figure 6a is a color-shaded DEM (1 m/pixel) of the same area generated from photogrammetric processing of a pair of stereo HiRISE images (ESP\_043896\_2055 and ESP\_044885\_2055). Figure 6b shows an elevation profile of a cone along the red dashed line in Figure 6a, derived from the 1-m resolution DEM. The profile indicates that the cone has a diameter of ~1 km, a height of ~70 m, and a wall slope of ~15°. The summit pit has a diameter of ~400 m and a depth of ~12 m.

### 3.3. Rock Abundance

Rocks can also be one of the most dangerous hazard for a lander and rover. Rock abundance (Golombek & Rapp, 1997), which is a measure of the cumulative fractional area covered by rocks with respect to the rock diameter, is a critical factor for landing-site evaluation (Golombek et al., 2003, 2012; Mastropietro et al., 2020; Pajola et al., 2017; Wu et al., 2018, 2020). Researchers have used ground-based images collected by cameras mounted on-board landers or rovers to analyze the rock abundance on Mars. Golombek and Rapp (1997) presented an exponential function of the rock abundance model based on rock measurements at the two Viking landing sites, which has been widely used to represent rock abundance on the Martian surface as it favorably matches the rock size-frequency distribution curves from real measurements taken from ground images at different landing sites, such as those of NASA's Mars missions: Mars Pathfinder (MPF) (Golombek & Rapp, 1997), Mars Exploration Rover (MER) (Golombek et al., 2003), and Mars Science Laboratory (Golombek et al., 2012).

However, direct measurements of rocks in images require very high-resolution imaging. High-resolution ground-based images of the Martian surface are only available from several existing landing sites, and high-resolution orbital images such as those from the HiRISE only cover a small portion of the surface. Thus, thermal emission data obtained from orbiters such as the Viking Infrared Thermal Mapper (IRTM) (Christensen, 1986) and the Mars Global Surveyor (MGS) Thermal Emission Spectrometer (TES) (Nowicki & Christensen, 2007) were also used to study rock abundances on the Martian surface (Pajola et al., 2019). The resulting rock-abundance maps provide global coverage, although the map resolution is low (e.g., 1 pixel/degree for the IRTM data). These maps nevertheless provide useful clues on rock abundances on large scales, which is important for landing-site evaluation over large areas. Golombek et al. (2012) stated that the IRTM rock-abundance values are very similar to the ground measurements at several landing sites, such as the two Viking landing sites, the MPF landing site, and the two MER landing sites. Therefore, this study also used the IRTM data to evaluate the rock abundance in the candidate landing region.

Figure 7a shows an IRTM rock-abundance map of the candidate landing region, which exhibits various rock abundances ranging from 1% to 23% over the region, with local clustered areas of low (the blue and cyan cells) and high (the red, brown, and yellow cells) rock abundances. To validate the IRTM rock abundance, we selected four local areas of low (marked as A and B in Figure 7a) and high (marked as C and D) rock abundances that also had HiRISE image coverage for analysis.

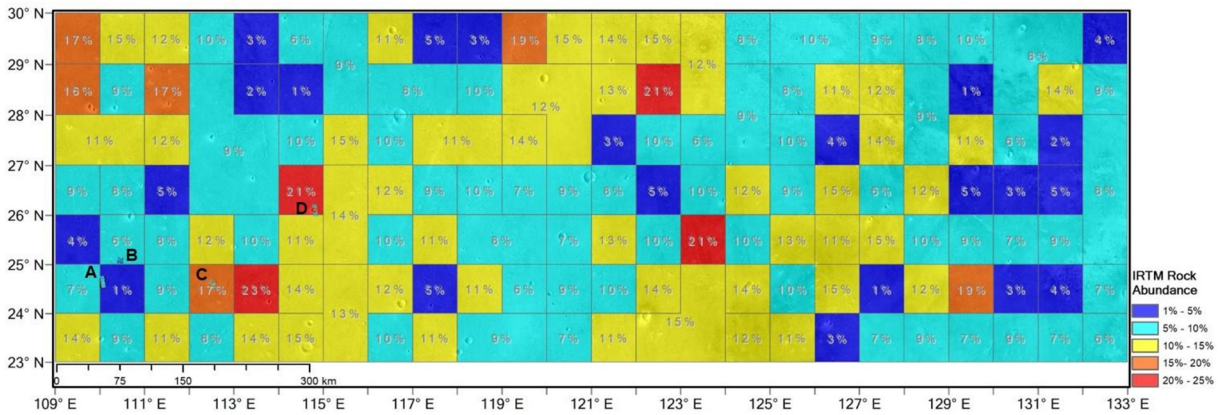
Rocks ( $\geq 1$  m in diameter) were detected on the HiRISE images using an automatic algorithm (Li & Wu, 2018) followed by manual checking. First, the shadows cast by rocks were detected based on the variations of brightness gradients along the illumination direction. Then, the rocks were represented by ellipses fitted from the clusters of shadow pixels. Finally, a manual checking process on the automatically detected rocks was conducted to exclude false detections and add omitted rocks, to guarantee the reliability of the detection results. The detected rocks were then used to estimate the rock abundance values by fitting the cumulative size-frequency distribution of rocks in a  $450 \times 450$  m window to the rock-abundance model. The rock-abundance values were sampled every 150 m to generate a rock-abundance map for each local area. Figure 7b shows the rock-abundance maps of the four local areas based on rock detection from HiRISE images. Figure 7c shows examples of rocks detected on the HiRISE images, and fitting of rock size-frequency distributions in local windows (black boxes on the HiRISE images) to the rock abundance model (Golombek & Rapp, 1997).

Table 2 summarizes the comparison between the rock abundances derived from the IRTM data and the HiRISE images at these four local areas, which shows that there is generally good consistency between the IRTM rock-abundance and the mean rock-abundance derived from HiRISE images. It can also be seen from Table 2 that areas C and D have large standard deviations. This is due to these two areas having large craters, around which the rock abundances are rather high, while the rock abundances for non-crater areas are much lower, as shown in Figure 7b. It is also noticeable that most rocks are concentrated around large craters, and that they are usually distributed on the crater wall or outside the craters in a radiating pattern.

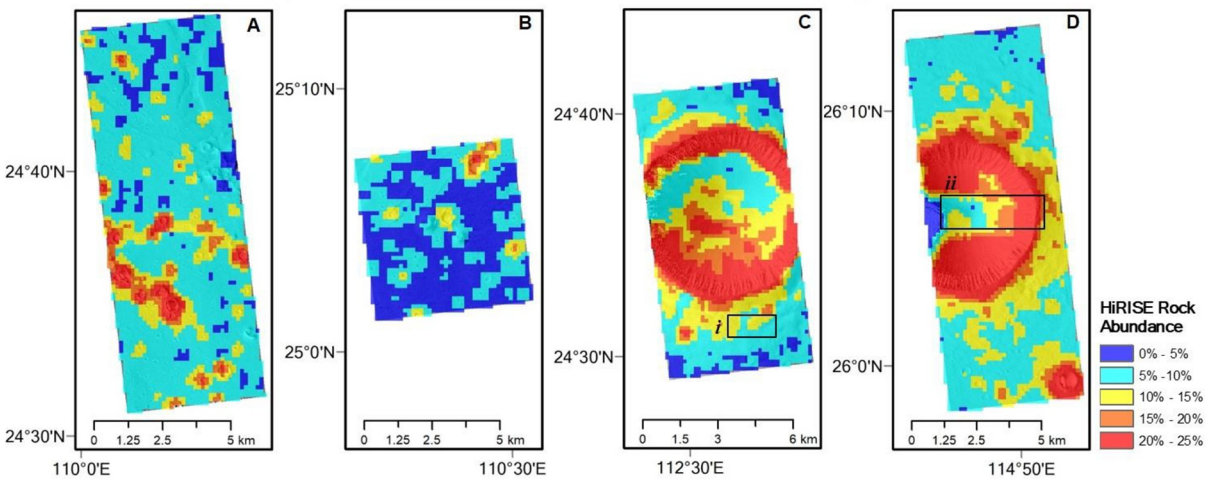
#### 4. Geological Units and Surface Ages of the Candidate Landing Region

In terms of the geological characteristics of the candidate landing region, we first investigated the geological units in the region based on the global geological map of Mars released by the U.S. Geological Survey (Tanaka et al., 2014). Geological units on the Martian surface are delineated based on characteristics that establish geological uniqueness, such as formational morphology, surface texture, infrared brightness, albedo characteristics, stratification, relative age, and spatial geological associations. According to the geological map of Mars (Tanaka et al., 2014), the candidate landing region was divided into four geological units as shown in Figure 8a, comprising two from the Amazonian period ( $< \sim 3$  Ga), namely an Amazonian and Hesperian volcanic (AHv) unit and an Amazonian volcanic (Av) unit, and two from the Late Hesperian period ( $\sim 3$ – $3.4$  Ga; Hartmann, 2005), namely a Late Hesperian lowland (lHl) unit and a Late Hesperian transition (lHt) unit.

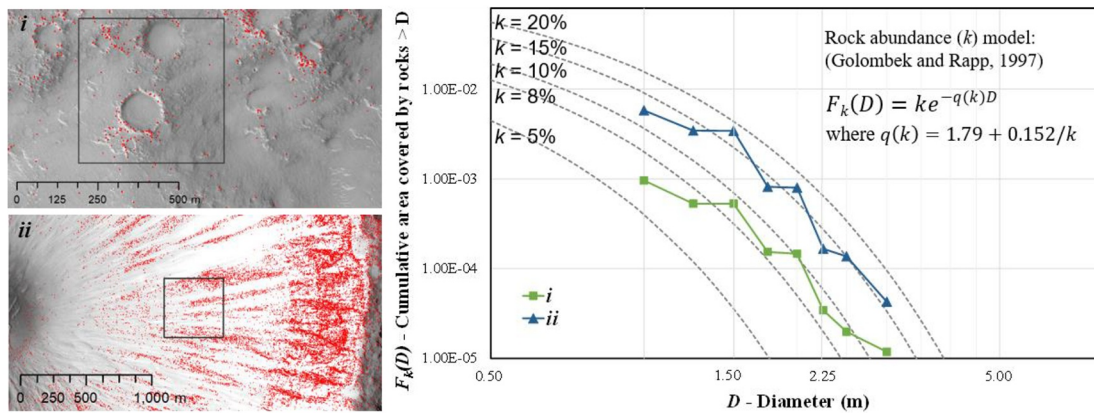
A crater size-frequency distribution (CSFD) analysis was conducted to estimate the specific surface ages of the geological units in the candidate landing region. Craters detected from the CTX image mosaic (as described previously) were used for this purpose. To minimize the influence of secondary craters on the



(a) IRTM rock abundance at the candidate landing region.



(b) HiRISE rock abundance at four sampling locations.



(c) Detected rocks on HiRISE images (ESP\_018446\_2050, ESP\_037566\_2065) (left) and fitting of rock size-frequency distributions to the rock abundance model (right).

**Figure 7.** Rock abundance at the candidate landing region. (a) Infrared Thermal Mapper (IRTM) rock abundance at the candidate landing region. (b) High Resolution Imaging Science Experiment (HiRISE) rock abundance at four sampling locations. (c) Detected rocks on HiRISE images (ESP\_018446\_2050, ESP\_037566\_2065) (left) and fitting of rock size-frequency distributions to the rock abundance model (right).

reliability of age estimation, only large craters ( $\geq 800$  m in diameter) were used, and possible secondary craters were manually identified and excluded. The identification of secondary craters was based on clues such as their distribution and visual distinctness from primary craters (Robbins & Hynes, 2014; Wu et al., 2019). For example, Figure 4a shows a few local regions of crater clusters with apparent radial patterns, which

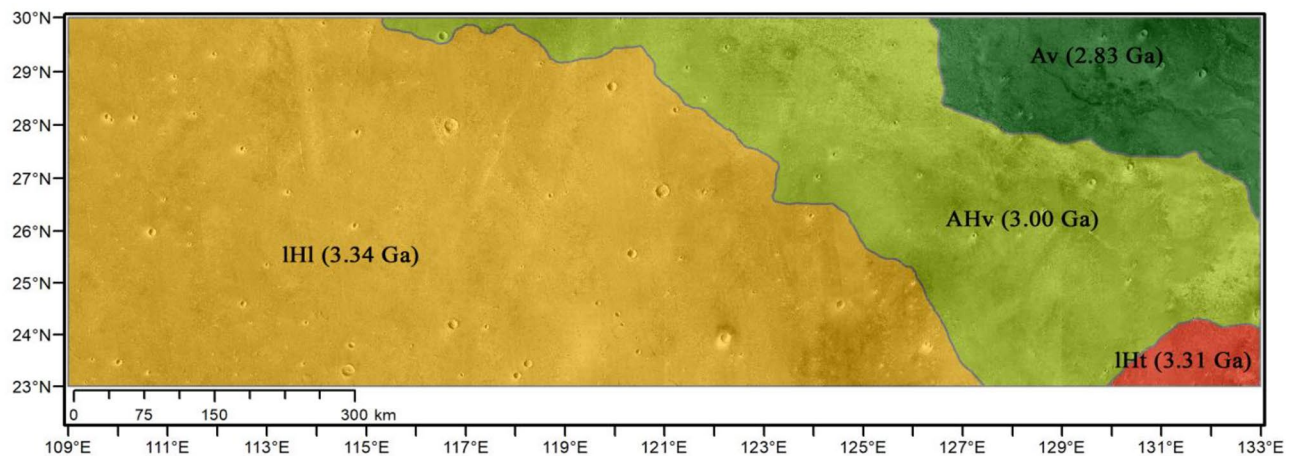
**Table 2**  
Comparison of IRTM and HiRISE Rock Abundance (RA) in Four Local Areas

Area	Center	IRTM RA	HiRISE RA		HiRISE image no.
			Mean	Std dev.	
A	(110.05°E, 24.64°N)	1%–7%	8%	4%	ESP_046929_2050
B	(110.45°E, 25.08°N)	1%–6%	5%	3%	ESP_044885_2055
C	(112.52°E, 24.59°N)	17%	17%	14%	ESP_018446_2050
D	(114.81°E, 26.10°N)	11%–21%	17%	15%	ESP_037566_2065

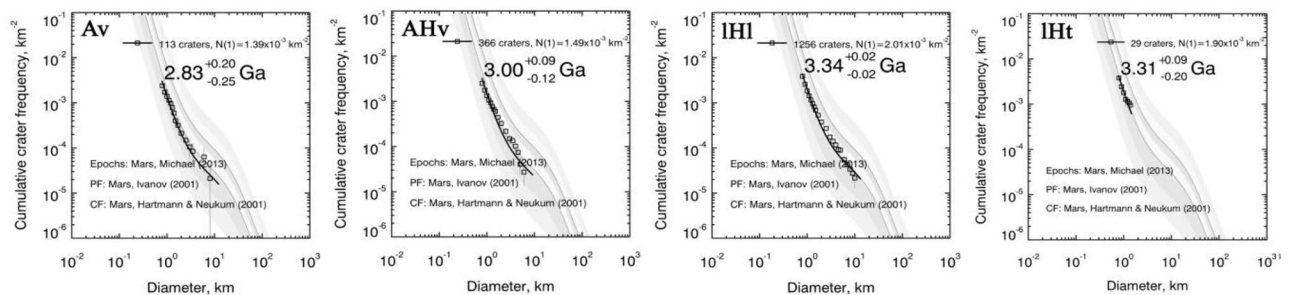
Abbreviations: IRTM, Infrared Thermal Mapper; HiRISE, High Resolution Imaging Science Experiment.

might be secondary craters of some primary craters in the far distance. After removing possible secondary craters, the surface ages of the geological units in the candidate landing region were then estimated using CraterStats software (Michael et al., 2010) based on the crater chronology function (Hartmann & Neukum, 2001), as shown in Figure 8a. Figure 8b shows the cumulative crater size-frequency plots for each unit. The shaded regions on the plots indicate different Martian epochs (Ivanov, 2001; Hartmann & Neukum, 2001; Tanaka et al., 2014), including Late, Middle, and Early Amazonian; Late and Early Hesperian; and Late, Middle, and Early Noachian, from left to right.

Our results are consistent with the geological-time division given by Tanaka et al. (2014), but provide a more specific chronological sequence of the four geological units. The oldest is the IHI unit ( $3.34^{+0.02}_{-0.02}$  Ga), representing a lowland unit on Utopia Planitia, which covers 61% of the candidate landing region in its



(a) The geological units and their estimated ages.



(b) Crater size-frequency plot for each unit.

**Figure 8.** Geological units and their estimated surface ages in the candidate landing region. (a) The geological units and their estimated ages and (b) Crater size-frequency plot for each unit.

western part. The lHt unit ( $3.31_{-0.20}^{+0.09}$  Ga), located at the south-eastern corner of the candidate landing region, is slightly younger than the lHl unit, which is close to the boundary between the lowlands in the north and the highlands in the southern hemisphere. The AHv and Av units are younger at  $3.00_{-0.12}^{+0.09}$  Ga and  $2.83_{-0.25}^{+0.20}$  Ga, respectively. These two units are volcanic units that likely formed from the lava flows and pyroclastic deposits from the nearby Elysium Mons in the east. The Av unit is younger than the AHv unit, possibly due to the subsequent hydro-interactions with the pyroclastic deposits, as many long channels are visible in the Av unit (also refer to the northeastern part of the color-shaded DEM shown in Figure 2a).

## 5. Evaluation of the Candidate Landing Region

### 5.1. Joint Topographic and Geomorphological Analysis for Surface Hazard Evaluation

The topographic (elevations and slopes) and geomorphological (distributions of craters, cones, and rocks) characteristics are important engineering considerations in landing site evaluation, to avoid hazards during touchdown of the lander and ensure better maneuverability of the rover. As described previously, the candidate landing region overall has a low elevation around  $-4,230$  m, which is favored for sufficient atmosphere to slow the lander during the descent phase. This paper further analyzes the slopes, crater density, cone density, and rock abundance over the candidate landing region for surface hazard evaluation. It should be noted that, the candidate landing region has relatively homogenous thermal inertia ( $246 \text{ Jm}^{-2}\text{s}^{-0.5} \text{ K}^{-1}$  in average with a standard deviation of  $32 \text{ Jm}^{-2}\text{s}^{-0.5} \text{ K}^{-1}$ ) and albedo (0.21 in average with a standard deviation of 0.02) based on the global thermal inertia and albedo maps (Putzig et al., 2005), which satisfies the engineering requirements well. Therefore, they are not included in the following analysis.

First, a surface slope constraint of  $\leq 8^\circ$  at a baseline of 4 m is imposed to ensure the stability of the lander during touchdown. This requirement is inherited from the successful Chang'E-3 (Wu et al., 2014) and Chang'E-4 (Wu et al., 2020) lunar soft-landing missions. The slope map of the candidate landing region shown in Figure 2c is classified into two categories:  $\leq 8^\circ$  and  $> 8^\circ$ , and the classified slope map is shown in Figure 9a. In the candidate landing region, 98% (blue areas) have slopes of  $\leq 8^\circ$ , and the other 2% (red areas) have slopes of  $> 8^\circ$ , mainly distributed around craters, channels, and ridges.

Second, for crater distribution, a lower crater density is preferred, as the internal slopes and protuberant rims of craters are potential hazards for safe landing. Places of high crater densities will lead to reduced flexibility of hazard avoidance during the descent phase of the lander. Besides, the lander should avoid landing in any small craters to allow the maximum maneuvering capability of the rover. Among all the detected craters ( $\geq 200$  m in diameter) in the candidate landing region, 88% of them have diameters of 200–400 m. Taking an average crater diameter of 300 m for consideration, 70 craters will cover an area of about  $5 \text{ km}^2$ , which accounts for 5% of the unit area of  $100 \text{ km}^2$  used for generating the crater density map. Therefore, this study selects a crater density of 70 craters ( $\geq 200$  m) per  $100 \text{ km}^2$  as a constraint for classification of the crater density map, which indicates a 5% risk for the lander to land in a crater ( $\geq 200$  m). The classified crater density map is shown in Figure 9b. Ninety-five percentage (blue areas) of the region have crater densities less than the constraint, and the remaining 5% (purple areas) have crater densities larger than the constraint. It should be noted that, this study focuses on craters  $\geq 200$  m in diameter; while smaller craters will have higher densities, and the actual risk for the lander to land in a crater might be higher. Nevertheless, this analysis is meaningful, as we are interested in the evaluation of the landing region of relatively favorable conditions of crater density on large scales.

Third, a similar strategy is used to evaluate the cone densities. The detected pitted cones in the candidate landing region have an average diameter of 550 m. Twenty one cones will cover an area of about  $5 \text{ km}^2$ , which accounts for 5% of the unit area of  $100 \text{ km}^2$  used for generating the cone density map. Therefore, a constraint of 21 cones per  $100 \text{ km}^2$  is used for classification of the cone density map, which indicates a 5% risk for the lander to land in an area with a cone. Figure 9c shows the classified cone density map. 99.3% (blue areas) of the region have cone densities less than the constraint. Only several segmented places (brown areas) located close to the southwestern and northeastern corners of the region have high cone densities.

Forth, regarding the rock abundance, the constraint on rock abundance is related to the ability to tolerate rocks while landing as well as roving. Seven percentage is considered as the upper ceiling of rock abundance

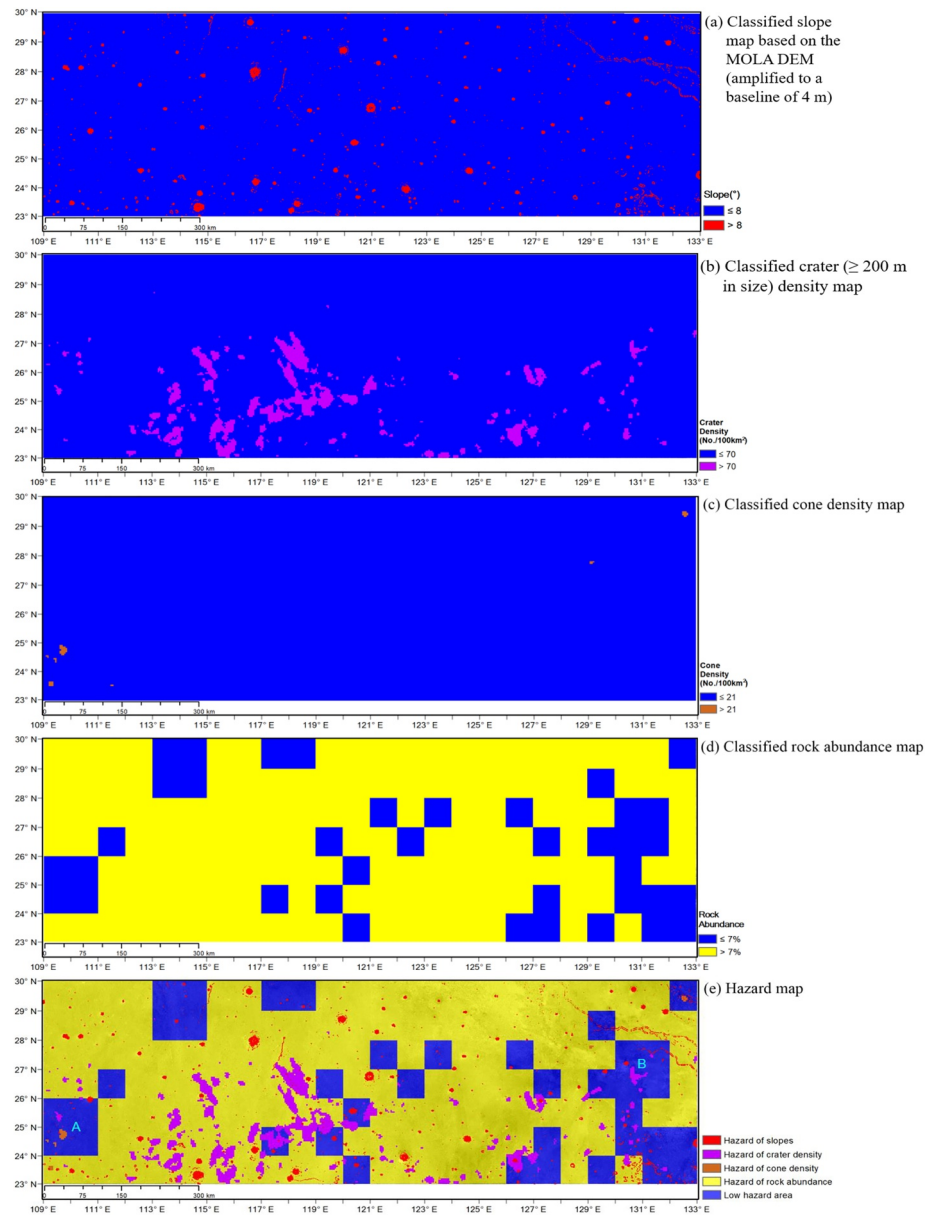


**Figure 9.** Joint topographic and geomorphological analysis for surface hazard evaluation. (a) Classified slope map based on the MOLA digital elevation model (amplified to a baseline of 4 m), (b) Classified crater ( $\geq 200$  m in size) density map, (c) Classified cone density map, (d) Classified rock abundance map and (e) Hazard map.

for a favorable landing site, considering the probability of encountering a rock hazard during landing and the rover traverse performance. The IRTM rock abundance map of the region is classified into two categories:  $\leq 7\%$  and  $> 7\%$ , as shown in Figure 9d. About 21% (blue areas) of the region have rock abundances  $\leq 7\%$ , and about 79% (yellow areas) of the region have rock abundances  $> 7\%$ .

Finally, combining the above constraints of slopes, crater density, cone density, and rock abundance, a hazard map of the candidate landing region is generated through an overlay analysis of each classified map, as shown in Figure 9e. It shows the distribution of local areas with relatively large slopes (red), crater densities (purple), cone densities (brown), and rock abundance (yellow). These local areas are considered to be unfavorable for a safe landing. The blue areas in Figure 9e indicate local areas of relatively low hazard, which could be potential landing sites.

## 5.2. Scientific Implications

Remote sensing and in situ investigations of the candidate landing region will address the scientific objectives of the mission, in terms of Martian morphology, geology, mineralogy, and water-ice distribution. The investigations will also help to update our knowledge about several important scientific questions on Mars, for example, the existence and history of water/ice and the magmatism characteristics on Mars.

Researchers suggested that Utopia Planitia possibly contained ponding water/ice in ancient times based on various clues (Chapman, 1994; Ivanov et al., 2014; McGill, 1989; Scott et al., 1992). McGill (1989) described the existence of a circular depression buried beneath Utopia Planitia, representing a very large impact basin. Scott et al. (1992) noted the evidence for a lacustrine basin in Utopia and suggested the occurrence of water/ice processes in the basin. Chapman (1994) suggested the existence of a frozen paleolake in Utopia Planitia as recently as 1.8 billion years ago, based on a basal scarp around the northwest flank of Elysium Mons and geomorphological features such as hyaloclastic ridges and hills, table mountains, and fluvial channels. Ivanov et al. (2014) investigated the morphology of impact craters and mud volcanism in Utopia Planitia, and stated the likely existence of water/ice in Late Hesperian period. In situ investigations at several possible landing sites with low hazard in the candidate landing region may provide new insights into the existence and history of water/ice in this region. Examples of these possible landing sites include the westernmost blue box and the large blue box close to the middle-eastern boundary of the region, as marked by “A” and “B” in Figure 9e. There are abundant fresh craters observed in these local areas from our crater mapping identification. These fresh impact craters offer exposures of less dusty materials, and provide opportunities to explore the mineralogical compositions from remote sensing data (Viviano et al., 2019). Our preliminary investigation based on the spectral analysis of observations from the Compact Reconnaissance Imaging Spectrometer for Mars (CRISM) at several fresh craters with sizes of kilometers in the region has revealed an abundance of hydrous minerals inside or around the craters. Figure 10 shows an example of detected hydrous minerals from the CRISM data around a fresh crater (about 7 km in size) located in the local area “B.” Access to these fresh craters by the rover and in situ measurements by its onboard multispectral camera will help to confirm and discover hydrous minerals of different types. Moreover, there are several fluvial channels across the area. Possible access to these channels by the rover may provide useful information about the existence of past water/ice there and the formation and history of these channels. The possible access of hydrous minerals in the candidate landing region will be valuable for the search for water/ice and evidence of past life. Hydrous minerals are produced by the hydrothermal alteration and weathering of primary basaltic minerals on Mars (Ehlmann et al., 2011; Schwenzer & Kring, 2009). Some of the mineral classes may have formed in environments that are suitable (i.e., containing sufficient water and at the correct pH) for life to evolve (Farmer & Des Marais, 1999). The investigation of hydrous minerals in the candidate landing region will also be useful for determining the hydrothermal evolution of the region.

The abundance of pitted cones in the candidate landing region is also of particular interest. These cones are mainly distributed in the late Hesperian lowland (IHI) unit (refer to Figures 5 and 8) in the southern area. There are several hypotheses for the origin of these cones. One is rootless cones similar to those found in Iceland on Earth, which were formed due to explosive interactions between surficial lavas and near-surface groundwater (Bruno et al., 2006). Hydro-volcanic interactions between ascending magma and subsurface water or water ice may explain the formation of these rootless cones on Mars (Brož & Hauber, 2013). Other hypotheses include, for example, mud volcanism (Farrand et al., 2005; Skinner & Tanaka, 2007) and terrestrial Maars (White & Ross, 2011). Farrand et al. (2005) noticed morphological differences of pitted cones from south to north in the north plain, and suggested more water was available at the time and locations of the eruptive processes that formed the northern cones. Ivanov et al. (2014) studied etched flows around the central portion of Utopia Planitia, and stated that the morphology and pattern of degradation of these etched flows were inconsistent with lava and, instead, due to mud volcanism. There are abundant cones in the local area “A” as shown in Figure 9e. Closer access by the rover to some of these pitted cones in the area may identify important features for detecting the presence or signature of volatiles (i.e., water or ice) in the near-surface environment on Mars.

Mineralogic investigation on the volcanic unit related to the nearby Elysium Mons, for example, the local area “B” on the Amazonian and Hesperian volcanic (AHv) unit in the eastern part of the candidate landing region as shown in Figure 9e, will provide direct measurements of mineralogic compositions of the surface

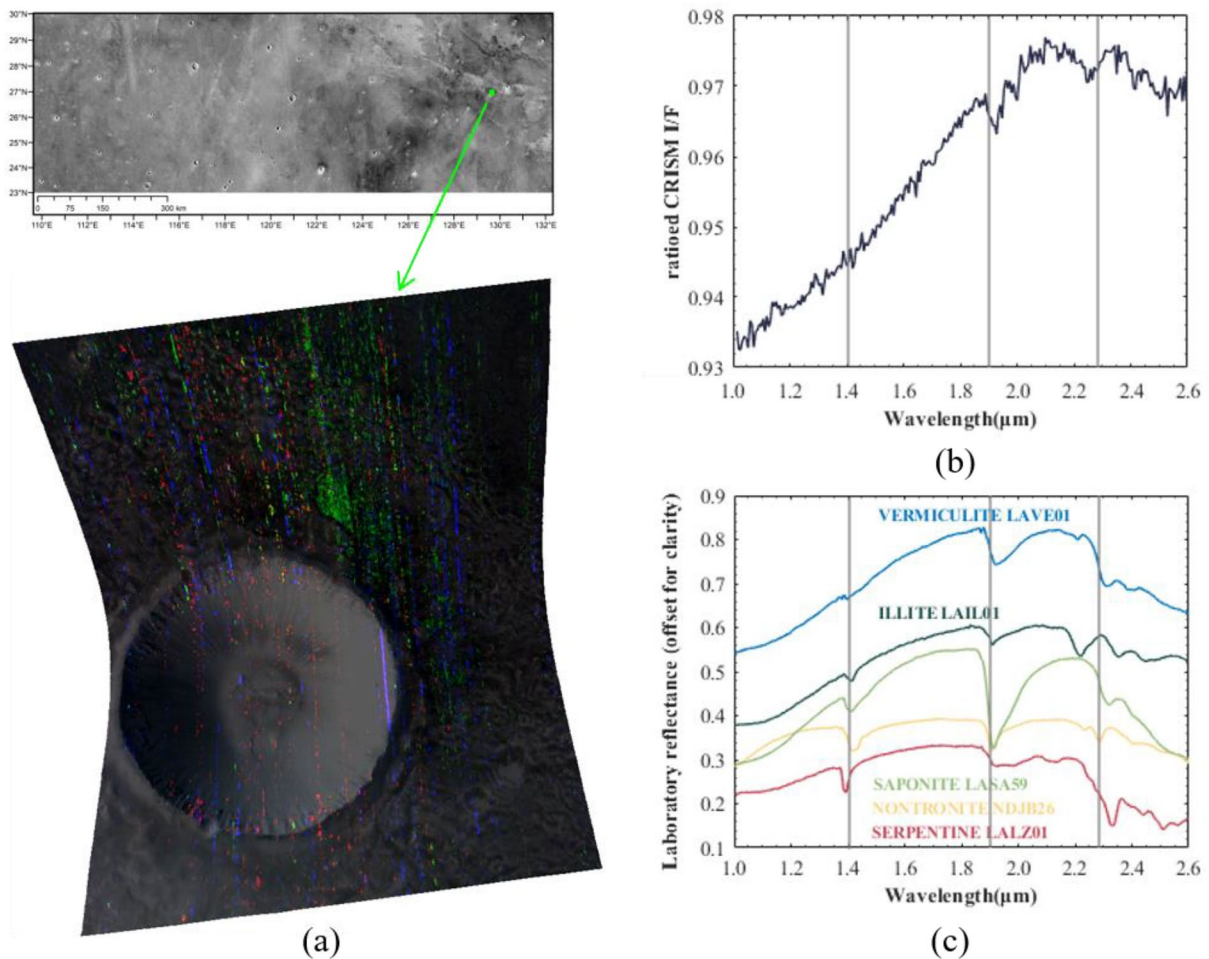


**Figure 10.** An example of hydrous minerals detected from Compact Reconnaissance Imaging Spectrometer for Mars (CRISM) data in the candidate landing region. (a) The CRISM image (FRT000093B3) showing a fresh crater of  $\sim 7$  km in diameter and the CRISM mineral parameter map (Fe/Mg clay minerals in red: D2300, Olivine minerals in green: OLINDEX3, Al clay minerals in blue: BD2210\_2); (b) Rationed CRISM I/F spectra; (c) Library spectra of clay minerals (illite, nontronite, saponite, serpentine, and vermiculite) for reference. The gray lines show absorptions at wavelengths of 1.4, 1.9, and 2.28  $\mu\text{m}$ .

materials. They will offer new ground truth about the volcanism on Mars (Viviano et al., 2019). These new data, together with existing knowledge (Susko et al., 2017), will facilitate a better understanding of the geochemical properties and temporal sequences of the lava fields of Elysium Mons, which will afford new insights into the magmatic processes and mantle heterogeneity on Mars.

## 6. Conclusions

In this study, we described our efforts for selection and characterization of the Utopia Planitia candidate landing region for Tianwen-1, China's first mission to Mars. The region has a low elevation ranging from  $-6,038$  to  $-3,275$  m, with an average elevation of  $-4,230$  m. The surface slopes of the region have an average of  $4.6^\circ$ , with 98% of the region having slopes of less than  $8^\circ$ . Large slopes are mainly distributed around craters, channels, and ridges. A total of 153,183 craters with diameters ranging from 200 m to 15 km were detected in the region, with 88% of them having diameters of 200–400 m. The region has an average crater density of about 28 craters ( $\geq 200$  m in diameter) per 100  $\text{km}^2$ , with several clusters of high crater densities distributed around the center of the region. A total of 2,503 pitted cones with diameters ranging from 40 m to 1.7 km were recognized in the region, with an average diameter of 550 m. They are distributed mainly in the southern part of the region, with a density of approximately 6.6 cones per  $\text{km}^2$  in representative local areas. The region has rock abundances ranging from 1% to 23% based on the IRTM data. Measurements

of rocks on HiRISE images at four local areas in the region indicate a generally good consistency between the IRTM rock-abundance and the mean rock-abundance derived from HiRISE images. The region comprises four geological units, with their specific surface ages estimated through CSFD analysis. The IHL unit ( $3.34^{+0.02}_{-0.02}$  Ga), representing a lowland unit on Utopia Planitia, covers 61% of the candidate landing region in its western part. There are two volcanic units, the AHv unit ( $3.00^{+0.09}_{-0.12}$  Ga) and Av unit ( $2.83^{+0.20}_{-0.25}$  Ga), located in the northeastern part of the region. There is also a small IHT unit ( $3.31^{+0.09}_{-0.20}$  Ga) located in the southeastern corner of the region.

Combining the engineering constraints on surface slopes, crater density, cone density, and rock abundance, a hazard map of the candidate landing region is generated for landing site evaluation. Based on the results, we further discuss the potential scientific outcomes from the exploration in this region. Two local areas (marked by "A" and "B" in Figure 9e) in the candidate landing region are highlighted for their low hazard considering engineering safety and scientific significance in terms of the existence and history of water/ice and the magmatism characteristics on Mars. The findings and results from this research will be helpful for the mission plan and maximization of the scientific returns from Tianwen-1, and complement existing Martian scientific research.

## Data Availability Statement

The MRO CTX and HiRISE data are available at the Mars Image Explorer (<https://viewer.mars.asu.edu/viewer/ctx#T=0>). The generated results of craters, cones, rocks, and geological units are available at Zenodo (<http://doi.org/10.5281/zenodo.3972675>).

## Acknowledgments

This work was funded by the China Academy of Space Technology (Project No: 17CPIT/HK0103) and grants from the Research Grants Council of Hong Kong (RIF Project No: R5043-19, Project No: PolyU 15210520). The authors would like to thank all those who worked on the archive of the datasets to make them publicly available.

## References

- Brady, T., Robertson, E., Epp, C., Paschall, S., & Zimpfer, D. (2009). Hazard detection methods for lunar landing. In *Proceedings of the 2009 IEEE Conference on Aerospace* (pp. 1–8).
- Brož, P., & Hauber, E. (2013). Hydrovolcanic tuff rings and cones as indicators for phreatomagmatic explosive eruptions on Mars. *Journal of Geophysical Research: Planets*, *118*, 1656–1675.
- Bruno, B. C., Fagents, S. A., Hamilton, C. W., Burr, D. M., & Baloga, S. M. (2006). Identification of volcanic rootless cones, ice mounds, and impact craters on Earth and Mars: Using spatial distribution as a remote sensing tool. *Journal of Geophysical Research*, *111*, E6. <https://doi.org/10.1029/2005je002510>
- Chapman, M. G. (1994). Evidence, age, and thickness of a frozen paleolake in Utopia Planitia, Mars. *Icarus*, *109*(2), 393–406. <https://doi.org/10.1006/icar.1994.1102>
- Christensen, P. R. (1986). The spatial distribution of rocks on Mars. *Icarus*, *68*(2), 217–238. [https://doi.org/10.1016/0019-1035\(86\)90020-5](https://doi.org/10.1016/0019-1035(86)90020-5)
- Dong, J., Sun, Z., Rao, W., Jia, Y., Wang, C., & Chen, B. (2019). Mission profile and design challenges of Mars landing exploration. In B. Wu, K. Di, J. Oberst, & I. Karachetseva (Eds.), *Planetary remote sensing and mapping* (pp. 75–87). Taylor & Francis Group/CRC Press.
- Ehlmann, B. L., Mustard, J. F., Murchie, S. L., Bibring, J.-P., Meunier, A., Fraemn, A. A., & Langevin, Y. (2011). Subsurface water and clay mineral formation during the early history of Mars. *Nature*, *479*, 53–60. <https://doi.org/10.1038/nature10582>
- Erkeling, G., Reiss, D., Hiesinger, H., Poulet, F., Carter, J., Ivanov, M. A., et al. (2012). Valleys, paleolakes and possible shorelines at the Libya Montes/Isidis boundary: Implications for the hydrologic evolution of Mars. *Icarus*, *219*, 393–413. <https://doi.org/10.1016/j.icarus.2012.03.012>
- Farmer, J. D., & Des Marais, D. J. (1999). Exploring for a record of ancient Martian life. *Journal of Geophysical Research*, *104*(E11), 26977–26995. <https://doi.org/10.1029/1998je000540>
- Farrand, W. H., Gaddis, L. R., & Keszthelyi, L. (2005). Pitted cones and domes on Mars: Observations in Acidalia Planitia and Cydonia Mensae using MOC, THEMIS, and TES data. *Journal of Geophysical Research*, *110*, E05005. <https://doi.org/10.1029/2004je002297>
- Frey, H. M., & Jarosewich, M. (1982). Subkilometer Martian volcanoes: Properties and possible terrestrial analogs. *Journal of Geophysical Research*, *87*, 9867–9879. <https://doi.org/10.1029/jb087ib12p09867>
- Golombek, M., Grant, J., Kipp, D., Vasavada, A., Kirk, R., Ferguson, R., et al. (2012). Selection of the Mars Science Laboratory landing site. *Space Science Reviews*, *170*, 641–737. <https://doi.org/10.1007/s11214-012-9916-y>
- Golombek, M. P., Haldemann, A. F. C., Forsberg-Taylor, N. K., Dimaggio, E. N., Schroeder, R. D., Jakosky, B. M., et al. (2003). Rock size-frequency distributions on Mars and implications for Mars Exploration Rover landing safety and operations. *Journal of Geophysical Research*, *108*(E12). <https://doi.org/10.1029/2002je002035>
- Golombek, M. P., & Rapp, D. (1997). Size-frequency distributions of rocks on Mars and Earth analog sites: Implications for future landed missions. *Journal of Geophysical Research: Planets*, *102*(E2), 4117–4129. <https://doi.org/10.1029/96je03319>
- Grant, J. A., Golombek, M. P., Wilson, S. A., Farley, K. A., Williford, K. H., & Chen, A. (2018). The science process for selecting the landing site for the 2020 Mars rover. *Planetary and Space Science*, *164*, 106–126. <https://doi.org/10.1016/j.pss.2018.07.001>
- Hartmann, W. K. (2005). Martian cratering 8: Isochron refinement and the chronology of Mars. *Icarus*, *174*, 294–320. <https://doi.org/10.1016/j.icarus.2004.11.023>
- Hartmann, W. K., & Neukum, G. (2001). Cratering chronology and the evolution of Mars. In *Chronology and evolution of Mars* (pp. 165–194). Springer. [https://doi.org/10.1007/978-94-017-1035-0\\_6](https://doi.org/10.1007/978-94-017-1035-0_6)
- Hu, H., Wu, B., & Chen, L. (2019). Color balancing and geometrical registration of high-resolution planetary imagery for improved orthographic image mosaicking. *Planetary and Space Science*, *178*, 104719. <https://doi.org/10.1016/j.pss.2019.104719>

- Ivanov, B. A. (2001). Mars/Moon cratering rate ratio estimates. *Space Science Reviews*, 96(1–4), 87–104. [https://doi.org/10.1007/978-94-017-1035-0\\_4](https://doi.org/10.1007/978-94-017-1035-0_4)
- Ivanov, M. A., Hiesinger, H., Erkeling, G., & Reiss, D. (2014). Mud volcanism and morphology of impact craters in Utopia Planitia on Mars: Evidence for the ancient ocean. *Icarus*, 228, 121–140. <https://doi.org/10.1016/j.icarus.2013.09.018>
- Ivanov, M. A., Slyuta, E. N., Grishakina, E. A., & Dmitrovskii, A. A. (2020). Geomorphological Analysis of ExoMars candidate landing site Oxia Planum. *Solar System Research*, 54(1), 1–14. <https://doi.org/10.1134/s0038094620010050>
- Jia, Y., Sun, Z., Zheng, Y., Li, H., Tao, Z., Zhang, T., & Tian, H. (2020). Overview on development of planetary rover technology. *Journal of Deep Space Exploration*, 7(5), 419–427.
- Li, Y., & Wu, B. (2018). Analysis of rock abundance on lunar surface from orbital and descent images using automatic rock detection. *Journal of Geophysical Research: Planets*, 123, 1061–1088. <https://doi.org/10.1029/2017je005496>
- MacKay, J. R. (1998). Pingo growth and collapse, Tuktoyaktuk Peninsula area, western arctic coast, Canada: A long-term field study. *Géographie Physique et Quaternaire*, 52, 1–53.
- Mastropietro, M., Pajola, M., Cremonese, G., Munaretto, G., & Lucchetti, A. (2020). Boulder analysis on the Oxia Planum ExoMars 2022 Rover landing site: Scientific and engineering perspectives. *Solar System Research*, 54(6), 504–519. <https://doi.org/10.1134/s0038094620060040>
- McGill, G. E. (1989). Buried topography of Utopia, Mars: Persistence of a giant impact depression. *Journal of Geophysical Research*, 94(B3), 2753–2759. <https://doi.org/10.1029/jb094ib03p02753>
- McGowan, E. M., & McGill, G. E. (2007). Spatial correlation of putative water related features in Cydonia Mensae and southern Acidalia Planitia. In *Seventh International Conference on Mars*.
- Michael, G. G., & Neukum, G. (2010). Planetary surface dating from crater size-frequency distribution measurements: Partial resurfacing events and statistical age uncertainty. *Earth and Planetary Science Letters*, 294(3–4), 223–229. <https://doi.org/10.1016/j.epsl.2009.12.041>
- Nowicki, S., & Christensen, P. (2007). Rock abundance on Mars from the thermal emission spectrometer. *Journal of Geophysical Research*, 112, E05007. <https://doi.org/10.1029/2006je002798>
- Oehler, D. Z., & Allen, C. (2010). Evidence for pervasive mud volcanism in Acidalia Planitia, Mars. *Icarus*, 208, 636–657. <https://doi.org/10.1016/j.icarus.2010.03.031>
- Pajola, M., Rossato, S., Baratti, E., & Kling, A. (2019). Planetary mapping for landing sites selection: The Mars case study. In *Planetary Cartography and GIS, Lecture Notes in Geoinformation and Cartography* (pp. 175, 190). Springer. [https://doi.org/10.1007/978-3-319-62849-3\\_7](https://doi.org/10.1007/978-3-319-62849-3_7)
- Pajola, M., Rossato, S., Baratti, E., Mangili, C., Mancarella, F., McBride, K., & Coradini, M. (2016). The Simud-Tiu valles hydrologic system: A multidisciplinary study of a possible site for future Mars on-site exploration. *Icarus*, 268, 355–381. <https://doi.org/10.1016/j.icarus.2015.12.049>
- Pajola, M., Rossato, S., Baratti, E., Pozzobon, R., Quantin, C., Carter, J., & Thollot, P. (2017). Boulder abundances and size-frequency distributions on Oxia Planum-Mars: Scientific implications for the 2020 ESA ExoMars rover. *Icarus*, 296, 73–90. <https://doi.org/10.1016/j.icarus.2017.05.011>
- Pajola, M., Rossato, S., Carter, J., Baratti, E., Pozzobon, R., Erculiani, M. S., et al. (2016). Eridania Basin: An ancient paleolake floor as the next landing site for the Mars 2020 rover. *Icarus*, 275, 163–182. <https://doi.org/10.1016/j.icarus.2016.03.029>
- Pan, D., Li, D., Yuan, B., Jia, Y., Wang, R., & Zhang, Z. (2020). Dynamics modeling and simulation analysis of Mars Rover System. *Journal of Deep Space Exploration*, 7(5), 437–444.
- Putzig, N. E., Mellon, M. T., Arvidson, R. E., & Kretke, K. A. (2005). Global thermal inertia and surface properties of Mars from the MGS mapping mission. *Icarus*, 173, 325–341. <https://doi.org/10.1016/j.icarus.2004.08.017>
- Robbins, S. J., & Hynek, B. M. (2014). The secondary crater population of Mars. *Earth and Planetary Science Letters*, 400, 66–76. <https://doi.org/10.1016/j.epsl.2014.05.005>
- Schwenzer, S. P., & Kring, D. A. (2009). Impact-generated hydrothermal systems capable of forming phyllosilicates on Noachian Mars. *Geology*, 37, 1091–1094. <https://doi.org/10.1130/g30340a.1>
- Scott, D. H., Chapman, M. G., Rice, J. W., & Dohm, J. M. (1992). New evidence of lacustrine basins on Mars—Amazonis and Utopia Planitia. In *Proceedings of Lunar and Planetary Science* (pp. 53–62).
- Sefton-Nash, E., Gupta, S., Balme, M., Grindrod, P., Fawdon, P., Davis, J., et al. (2015). ExoMars 2018 Rover candidate landing sites: Aram Dorsum and the Hypanis Vallis Delta. In *European Planetary Science Congress 2015* (Vol. 27).
- Sejourné, A., Costard, F., Gargani, J., Soare, R. J., & Marmo, C. (2012). Evidence of an eolian ice-rich and stratified permafrost in Utopia Planitia, Mars. *Icarus*, 60, 248–254. <https://doi.org/10.1016/j.jps.2011.09.004>
- Skinner, J. A., Jr. & Tanaka, K. L. (2007). Evidence for and implications of sedimentary diapirism and mud volcanism in the southern Utopia highland-lowland boundary plain, Mars. *Icarus*, 186(1), 41–59. <https://doi.org/10.1016/j.icarus.2006.08.013>
- Smith, D. E., Zuber, M. T., Frey, H. V., Garvin, J. B., Head, J. W., Muhleman, D. O., et al. (2001). Mars orbiter laser altimeter: Experiment summary after the first year of global mapping of Mars. *Journal of Geophysical Research*, 106(E10), 23689–23722. <https://doi.org/10.1029/2000je001364>
- Susko, D., Karunatillake, S., Kodikara, G., Skok, J. R., Wray, J., Heldmann, J., et al. (2017). A record of igneous evolution in Elysium, a major Martian volcanic province. *Scientific Reports*, 7, 43177. <https://doi.org/10.1038/srep43177>
- Tanaka, K. L., Skinner, J. A., Jr, Dohm, J. M., Irwin, R. P., III, Kolb, E. J., Fortezzo, C. M., et al. (2014). Geologic map of Mars. In *US geological survey scientific investigations map 3292* (p. 48).
- Vaucher, J., Baratoux, D., Mangold, N., Pinet, P., Kurita, K., & Grégoire, M. (2009). The volcanic history of central Elysium Planitia: Implications for Martian magmatism. *Icarus*, 204, 418–442. <https://doi.org/10.1016/j.icarus.2009.06.032>
- Viviano, C. E., Murchie, S. L., Daubar, I. J., Morgan, M. F., Seelos, F. P., & Plescia, J. B. (2019). Composition of Amazonian volcanic materials in Tharsis and Elysium, Mars, from MRO/CRISM reflectance spectra. *Icarus*, 328, 274–286. <https://doi.org/10.1016/j.icarus.2019.03.001>
- Wang, Y. R., & Wu, B. (2017). Improved large-scale slope analysis on Mars based on correlation of slopes derived with different baselines. In *International Archives of the Photogrammetry, Remote Sensing & Spatial Information Sciences* (p. 42).
- Wang, Y. R., & Wu, B. (2019). Active machine learning approach for crater detection from planetary imagery and digital elevation models. *IEEE Transactions on Geoscience and Remote Sensing*, 57(8), 5777–5789. <https://doi.org/10.1109/tgrs.2019.2902198>
- Wan, W. X., Wang, C., Li, C. L., & Wei, Y. (2020). China's first mission to Mars. *Nature Astronomy*, 4, 721. <https://doi.org/10.1038/s41550-020-1148-6>
- Werner, S. C. (2014). Moon, Mars, Mercury: Basin formation ages and implications for the maximum surface age and the migration of gaseous planets. *Earth and Planetary Science Letters*, 400, s54–65. <https://doi.org/10.1016/j.epsl.2014.05.019>
- White, J. D. L., & Ross, P.-S. (2011). Maar-diatreme volcanoes: A review. *Journal of Volcanology and Geothermal Research*, 201(1–4), 1–29. <https://doi.org/10.1016/j.jvolgeores.2011.01.010>

- Wu, B., Huang, J., Li, Y., Wang, Y., & Peng, J. (2018). Rock Abundance and Crater Density in the Candidate Chang'E-5 Landing Region on the Moon. *Journal of Geophysical Research: Planets*, *123*(12), 3256–3272. <https://doi.org/10.1029/2018je005820>
- Wu, B., Li, F., Hu, H., Zhao, Y., Wang, Y., Xiao, P., et al. (2020). Topographic and geomorphological mapping and analysis of the Chang'E-4 landing site on the far side of the Moon. *Photogrammetric Engineering & Remote Sensing*, *86*(4), 247–258. <https://doi.org/10.14358/pers.86.4.247>
- Wu, B., Li, F., Ye, L., Qiao, S., Huang, J., Wu, X., & Zhang, H. (2014). Topographic modeling and analysis of the landing site of Chang'E-3 on the Moon. *Earth and Planetary Science Letters*, *405*, 257–273. <https://doi.org/10.1016/j.epsl.2014.09.009>
- Wu, B., Wang, Y., Lin, T. J., Hu, H., & Werner, S. C. (2019). Impact cratering in and around the orientale basin: Results from recent high-resolution remote sensing datasets. *Icarus*, *333*, 343–355. <https://doi.org/10.1016/j.icarus.2019.06.018>
- Ye, P., Sun, Z., Rao, W., & Meng, L. (2017). Mission overview and key technologies of the first Mars probe of China. *Science China Technological Sciences*, *60*, 649–657. <https://doi.org/10.1007/s11431-016-9035-5>
- Zou, Y., Zhu, Y., Bai, Y., Wang, L., Jia, Y., Shen, W., et al. (2021). Scientific objectives and payloads of Tianwen-1, China's first Mars exploration mission. *Advances in Space Research*, *67*, 812–823. <https://doi.org/10.1016/j.asr.2020.11.005>